L~~ETTER~~ ~~TO THE~~ E~~DITOR~~

Are we witnessing ongoing planet formation in AB Aurigae?[*]

A showcase of the SPHERE/ALMA synergy

A. Boccaletti[1], E. Di Folco[2], E. Pantin[3], A. Dutrey[2], S. Guilloteau[2], Y. W. Tang[4], V. Piétu[5], E. Habart[6], J. Milli[8], T. L. Beck[7], and A.-L. Maire[9]

[1] LESIA, Observatoire de Paris, Université PSL, CNRS, Sorbonne Université, Univ. Paris Diderot, Sorbonne Paris Cité, 5 place Jules Janssen, 92195 Meudon, France
[2] Laboratoire d'Astrophysique de Bordeaux, Université de Bordeaux, CNRS, B18N, Allée Geoffroy Saint-Hilaire, 33615, Pessac, France
[3] Laboratoire CEA, IRFU/DAp, AIM, Université Paris-Saclay, Université Paris Diderot, Sorbonne Paris Cité, CNRS, F-91191 Gif-sur-Yvette, France
[4] Academia Sinica, Institute of Astronomy and Astrophysics, 11F of AS/NTU Astronomy-Mathematics Building, No.1, Sec. 4, Roosevelt Rd, Taipei, Taiwan
[5] IRAM, 300 rue de la piscine, Domaine Universitaire, 38406 Saint-Martin d'Hères, France
[6] Institut d'astrophysique spatiale, CNRS UMR 8617, Université Paris-Sud 11, Bât 121, 91405, Orsay, France
[7] Space Telescope Science Institute, 3700 San Martin Drive, Baltimore, MD, 21218, USA
[8] CNRS, IPAG, Univ. Grenoble Alpes, F-38000 Grenoble, France
[9] STAR Institute, Université de Liège, Allée du Six Août 19c, B-4000 Liège, Belgium

March 23, 2020

ABSTRACT

Context. Planet formation is supposed to occur in the first million years of a planetary system through various processes, which remain to be tested by means of observations.
Aims. With the recent discovery from ALMA of two gaseous spiral arms inside the ~120 au cavity, connected to dusty spirals, the famous protoplanetary disk around AB Aurigae presents a strong interest to investigate the mechanisms leading to giant planet formation. A candidate protoplanet located inside a spiral arm has been claimed from the same ALMA data.
Methods. We used SPHERE at the VLT to perform near-IR high contrast imaging of AB Aur in polarized and unpolarized light, in order to study the morphology of the disk and to search for signs of planet formation.
Results. SPHERE delivered the deepest images ever obtained for AB Aur in scattered light. Among the many structures yet to be understood, we identified not only the inner spiral arms, but we also resolved a feature in the form of a twist in the eastern spiral at a separation of about 30 au. The twist of the spiral is perfectly reproduced with a planet-driven density wave model when projection effects are accounted for. We measured an azimuthal displacement with respect to the counterpart of this feature in the ALMA data, which is consistent with Keplerian motion on a 4-yr baseline. Another point source is detected near the edge of the inner ring, which is likely the result of scattering as opposed to the direct emission from a planet photosphere. We tentatively derived mass constraints for these two features.
Conclusions. The twisted spiral pattern and its apparent orbital motion could well be the first direct evidence of a site of protoplanet formation.

Key words. Stars: individual (AB Aur) – Protoplanetary disks – Planet-disk interactions – Techniques: image processing – Techniques: high angular resolution

1. Introduction

Planets are believed to form in protoplanetary disks in a few million years. Images at all wavelengths exhibit many types of structures like asymmetries, clumps, rings, or spirals. Most of these features, which hypothetically betray the presence of planets via gravitational and/or hydrodynamical effects are observed in disks orbiting Herbig Ae/Be stars because of their suitable brightness, particularly in the NIR (see for instance Grady et al. 2001; Clampin et al. 2003; Fukagawa et al. 2006; Isella

et al. 2010; Christiaens et al. 2014). Planet formation is generally favored (Zhu 2015) against instabilities in a massive self-gravitating disk (Rice et al. 2005). In the early stage of planet formation, hydrodynamical simulations indicate that the accretion process generates at the planet location an inner and outer spiral pattern due to Lindblad resonances induced by disk-planet interactions (Gressel et al. 2013). While this crucial step is well documented by theoretical works (Dong et al. 2015; Bae & Zhu 2018), observational evidences are rare and not fully conclusive.

With a spectral type A0 ($2.4 \pm 0.2 M_{\odot}$, DeWarf et al. 2003), AB Aurigae is one of the closest ($d = 162.9 \pm 1.5$ pc, Gaia Collaboration et al. 2018), and one of the most intensively studied Herbig Ae star. Optical scattered light images of its protoplanetary disk have been obtained in the visible (Grady et al.
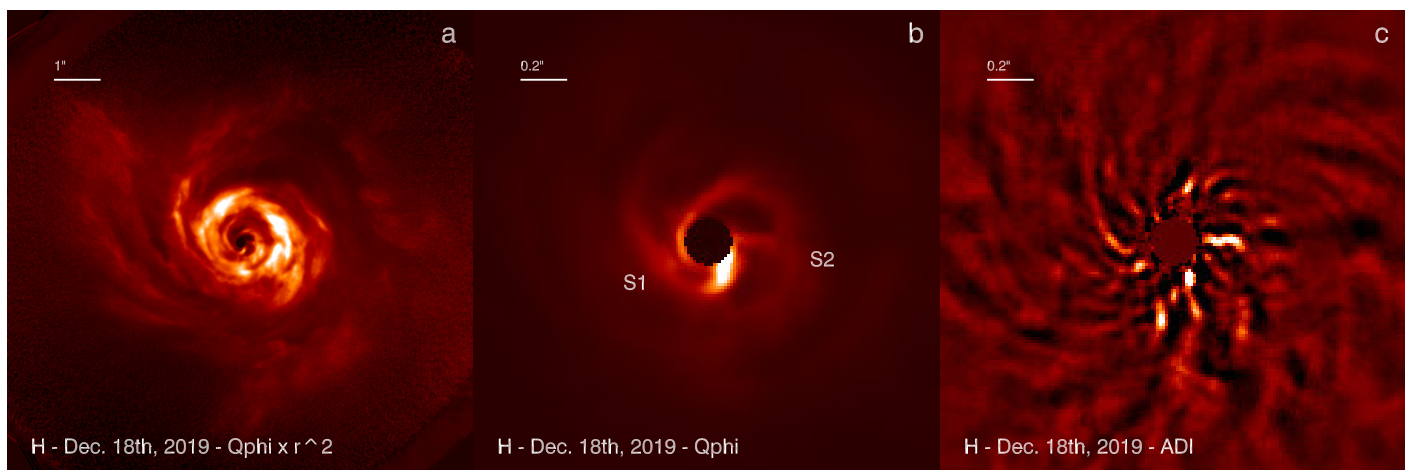
Fig. 1. Images of the AB Aur system obtained with SPHERE in polarized light (a, b) and unpolarized light (c). A large field of view (10″) is shown in panel a, where the polarized intensity has been multiplied with the square of the stellocentric distance to visually enhance the outer part of the disk. A narrower field of view (2″) is displayed in panel b where the inner spirals are labelled S1 and S2. Comparable ADI-processed image is shown in panel c for total intensity in the H band filter. North is up, east is left

1999; Fukagawa et al. 2004), and in the near IR (Perrin et al. 2009; Hashimoto et al. 2011), revealing a moderately inclined ($i \sim 30°$), flared disk, and prominent spiral patterns extending from 200 to 450 au. In fact, AB Aurigae exhibits among the most spectacular spirals imaged so far in scattered light and high-contrast polarimetric imaging.

Millimetric observations were also key to constrain the distribution of gas and dust in the AB Aur system. Using the IRAM interferometer, Piétu et al. (2005) reported the presence of a large CO and dust rotating disk with a central cavity of inner radius ~ 70 au. Surprisingly, Tang et al. (2012) found counter-rotating CO spirals in the outer disk, which has been explained by projection effects of accretion flows arising from above the disk midplane. The large accretion rate ($\sim 10^{-7} M_\odot$/yr, Salyk et al. 2013) measured for this 1 Myr object reinforces this interpretation.

More recently, Tang et al. (2017) studied the CO 2-1 and dust continuum distribution at very high angular scale (0.08″ or 13 au) using ALMA, and revealed two spectacular CO spirals residing inside the large disk cavity. The authors speculated that these spirals are driven by planet formation and could be generated by two planets respectively located at ∼30 and 60-80 au from the star. Motivated by these results, we have conducted VLT/SPHERE observations of the AB Aurigae system that we present in this letter. After describing the observations, we analyze the data and discuss the possible origin of the inner spiral pattern.

2. Observations

AB Aur (V=7.05, H=5.06, K=4.23) was observed with SPHERE (Beuzit et al. 2019) in polarimetry (Dec 2019) and in spectro-photometry (Jan 2020). The first data set was obtained with the infrared camera IRDIS (Dohlen et al. 2008; de Boer et al. 2020) using Pupil Tracking (PT) in the H band, which allows to retrieve at the same time the polarized intensity of the disk and the total intensity making use of Differential Polarimetric Imaging (DPI) and of Angular Differential Imaging (ADI). The second epoch used the `IRDIFS-EXT` mode of SPHERE, which combines IRDIS in the K1K2 filters, and the spectrograph (IFS, Claudi et al. 2008) in low resolution mode YJH (R=30), also processed with ADI. The observing log is provided in Table A.1.

Both DPI and ADI increase the contrast by rejecting the starlight, either using the fact that the stellar light is unpolarized or that off-axis objects rotate with the field in PT mode. While DPI provides unbiased polarimetric images of disks, ADI induces very strong photometric and astrometric artifacts owing to the self-subtraction effect (Milli et al. 2012). The data were processed at the SPHERE Data Center following Pavlov et al. (2008); Delorme et al. (2017); Maire et al. (2016). The calibrated data cubes were then processed with SpeCal for total intensity data (Galicher et al. 2018), and with a custom pipeline for polarimetric data. The latter were compared to the output of the IRDAP pipeline (van Holstein et al. 2020) and found in good agreement. The total intensity data were reduced with Principal Component Analysis (Soummer et al. 2012), while for polarimetry we calculated the azimuthal Stokes parameters Q_ϕ and U_ϕ maps following Schmid et al. (2006). The first epoch is significantly better in terms of starlight rejection hence the following sections are mostly based on these observations.

3. Disk morphology

The disk being moderately inclined, the ADI process strongly attenuates irremediably the disk signal (Fig. 1c). Therefore, the following description is based on the polarimetric H-band Q_ϕ image (Fig. 1a, b). The disk is visible all across the IRDIS 11″ × 11″ field of view. We identify three main regions: the dust ring, the outer spirals and the inner spirals.

The position of the ring detected with ALMA in the continuum (Tang et al. 2017) is shown in Fig. 2a. In the sub-mm, it encompasses an elliptical region oriented at 35° north to east, from a minimal radius of 0.77″ to a maximal separation of 1.19″, corresponding to a ring of ∼140 au on average (yellow ellipses in Fig. 2a). The aspect ratio is consistent with an inclination of 30°. In scattered light, the ring is not homogeneous with brighter parts in the west and the north-east, as opposed to the smooth 1.3 mm image which instead peaks to the southwest. SPHERE resolves some structures in the ring that were already reported in scattered light by Oppenheimer et al. (2008) and Hashimoto et al. (2011). In particular, the dip in polarimetry is also observed at PA=343° although the contrast is low and its visibility is mostly
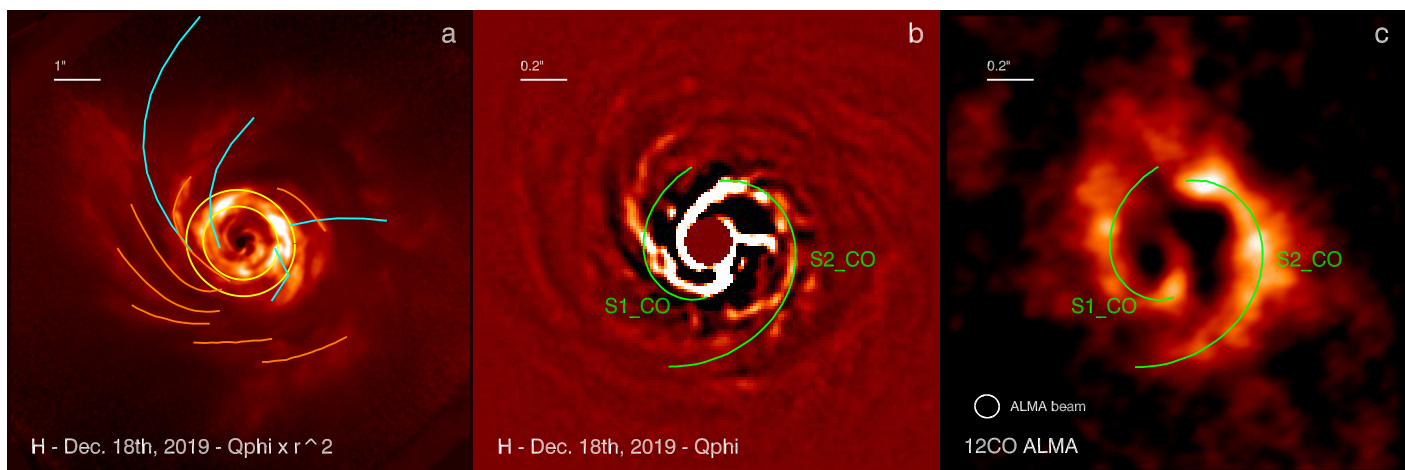
Fig. 2. Full field image in polarimetry (a) on top of which several structures previously detected are overlaid: Hashimoto et al. (2011) spirals (orange lines), out of plane accreting spirals from Tang et al. (2012) (blue lines), and the dust ring (yellow ellipses) from the 0.9-mm ALMA image (Tang et al. 2017). The inner spiral arms (S1_CO, S2_CO) detected by Tang et al. (2017) are superimposed to the SPHERE polarimetric image (b), and the ALMA CO map (c), in a 2″ field of view. North is up, east is left.

a matter of intensity cut. We do not detect any point-source at this location, confirming Perrin et al. (2009).

Outward of the ring there are several spiral-like structures, which given the sensitivity achieved with SPHERE DPI, could in fact be the trace of one single grand spiral with several ramifications. This pattern likely starts from the south and rolls clockwise while it gets broader with manyfold branches (Fig. 1a). It is particularly pronounced at the east and is very well matching all the spirals identified in 2009 H-band data by Hashimoto et al. (2011) at Subaru (orange lines in Fig. 2a), indicating no perceptible motion in 10 years, as already concluded by Lomax et al. (2016) on a shorter timescale. Therefore, this pattern is unlikely to be driven by planets inside the ring. Out-of-plane CO spirals (Tang et al. 2012), which have no obvious counterpart in scattered light, are indicated in cyan (Fig. 2a).

Inward of the ring ($< 0.6''$), we detect two main spirals (S1 and S2 in Fig. 1b) starting as close as the edge of the coronagraphic mask (about 95 mas in radius), and in good agreement with the CO spirals identified by Tang et al. (2017, green lines labelled S1_CO and S2_CO in Fig. 2b, c). The angular resolution brought by SPHERE evidences that the two inner spirals seem to intersect at the south of the star exactly at the location of an intensity peak ($\rho = 0.21''$, $PA = 177.7°$), which itself is found at a very similar position than the CO peak. S2 matches well the western CO spiral, while S1 seems to deviate from the eastern CO spiral. We suspect that this mismatch is due to the difference of angular resolution, which for ALMA is about 0.11″, while SPHERE provides in H band a resolution of 0.04″. As a consequence, it is difficult to disentangle S1 from S2 at the north in the CO map. S2 is more diffuse than S1 and appears larger in the west. High-pass filtering of the polarimetric image (Fig. 2b) shows higher complexity with clumps and several arms.

While the CO map contains a cavity inward of the CO spirals the SPHERE observations reveal a third component ($PA \sim 270°$ in Fig. 1b) connecting the center of the image to S2, as a kind of "bridge" of $25 - 30$ au long. This is not a post-processing artifact since this feature is seen both in the polarimetry image and in the total intensity ADI image, and was in fact already distinguishable in Hashimoto et al. (2011), but also in the gas line HCO$^+$ (Rivière-Marichalar et al. 2019). Whether it is a true connection or a projection effect cannot be determined with these observa-

tions alone. On each side of the "bridge" the polarized intensity is rather low, even lower than in between the spiral arms. Interestingly, in the direction of this feature the intensity of the spiral S2 and of the ring is fainter, possibly tracing a shadow pattern. If so, it will favor a feature near the midplane of the disk. Finally, S1 shows an increase of its width at $PA \sim 115°$ like a compact clump $\sim 0.12''$ long (Fig. 1b, 2b), Complementary images are displayed in Appendix A.

4. Point-like sources

Many structures are observed in the disk but two features have a strong interest. The first one (f1) is the strongest signal in Fig. 1b, and c, south of the coronagraphic mask edge, and a second one (f2) is a nearly point source further out to the north. Interestingly, both show up in DPI and ADI images (Fig. 3). They are also detected at the second epoch in total intensity (ADI), although with a much lower signal to noise ratio (Fig. A.1).

We extracted photometry and astrometry with SpeCal. The positions of the sources are based on the ADI reduction using the PCA 5 modes algorithm (Fig. 2b) and the negative fake planet injection method (for details see Galicher et al. 2018), but the values are consistent within error bars for all algorithms. f1 is located at $\rho = 0.160 \pm 0.006''$, $PA = 203.9 \pm 2.9°$. It coincides with the root of the eastern spiral identified as S1 in the ALMA image, where the two spirals seem to intersect. The shape of this feature in the Q_ϕ image (Fig. 3a) is remarkable and will be discussed in the next section. The second source, f2, lies at the very edge of the dust ring inside the cavity, in the prolongation of the eastern spiral. Its position is $\rho = 0.681 \pm 0.006''$, $PA = 7.6 \pm 1.8°$.

f1 is elongated while f2 is nearly point-like. This characteristic is confirmed by the photometric analysis. The contrast relative to the star derived from IRDIS data in the H band and measured at f1 is quite variable from one ADI reduction to another, ranging from $6.5 \pm 0.8 \times 10^{-4}$ to $6.8 \pm 0.6 \times 10^{-5}$, depending on the aggressiveness (ability to suppress the starlight) of the ADI algorithm.

In the K1K2 IRDIS image obtained at the second epoch, we also measured some variations with respect to the algorithm, but with a small difference of contrast between the two narrow band filters: $3.4 \pm 0.5 \times 10^{-4}$ and $4.3 \pm 0.5 \times 10^{-4}$ respectively. Whether
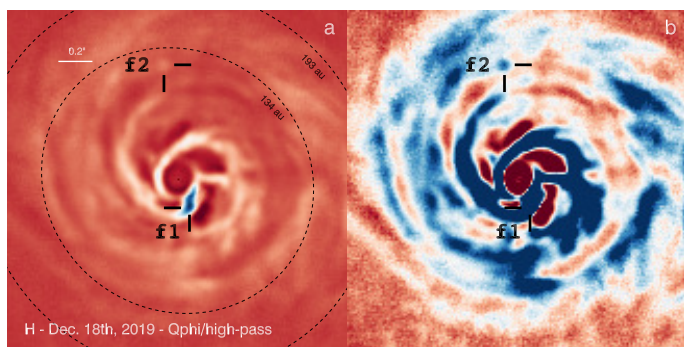
Fig. 3. Positions of features `f1` and `f2` overlaid on the polarimetric image shown for two intensity thresholds. The dusty ring is materialized with the dashed ellipses. For visualisation purpose the polarized intensity has been high-pass filtered and multiplied with the stellocentric distance.

it is indicative of a red color remains to be confirmed with higher quality data in the K band. Overall, we cannot consider the total intensity contrast measurements of `f1` reliable as it cannot be assimilated to a point source. On the contrary, `f2` has a stable contrast in the H band of $4.9 \pm 0.5 \times 10^{-6}$, and $4.8 \pm 0.8 \times 10^{-6}$ in K1K2, indicative of a bona-fide point source, but with a grey color. Photometric measurements with the IFS (not shown here) in the YJH bands are not much more conclusive regarding `f1`, while `f2` is actually not detected.

The fact that `f1` and `f2` are detected in polarimetry and total intensity strongly suggests that these signals cannot result from the photosphere of some protoplanets, but instead are likely the telltale of dust particles detected from scattering or from other thermally-induced mechanisms.

5. Spirals

The presence of spiral arms in protoplanetary disks has been usually associated to the indirect clues of planets provided that the disks are not massive enough to undergo self-gravity (Muto et al. 2012; Boccaletti et al. 2013; Benisty et al. 2015, for instance). This link with a gravitational perturber has never been definitely established, except for the prominent spiral arms in HD 100453, very likely launched by a stellar M-dwarf companion (Dong et al. 2016). In that respect, the ALMA observations of AB Aur (Tang et al. 2017) are likely the only case, together with GG Tau A (Phuong et al. 2020), to provide a strong suspicion for the presence of a protoplanet associated to spiral arms.

To model the morphology of the inner spirals we rely on the formulation of Muto et al. (2012) described in Appendix B. A direct fit of this analytical relation (Eq. B.1) onto the spiral positions was found too unstable given the difficulty to isolate the spine of the spiral arms against the other disk structures. Instead, we proceed with a manual adjustment of the theoretical spiral location taking into account the disk inclination ($i = 30°$), the disk Position Angle ($PA = 60°$), the gas disk vertical scale-height ($H_0 = 25$ au at 100 au) and the flaring index ($r^{1.2}$), following di Folco et al. (2009); Hashimoto et al. (2011); Tang et al. (2012); Li et al. (2016). Because the spirals are pressure bumps, they are localized at the disk surface and not in the mid-plane (Juhasz et al. 2015), we assume that the altitude of the disk layer at which the optical depth (τ_ν) is equal to one is $H(\tau = 1) = 1.5 \times H_0$. These values are used to project the analytical relation $\theta(r)$ onto the plane of the sky, but are known to some level of accuracy.

Therefore, the solutions presented here provide qualitative results, and may not be unique. We note in particular a degeneracy between the inclination, the disk scale-height, and the radial distance of the putative planet, whereas the flaring index has only a weak impact on the shape of the projected spiral.

To account for S1 we considered two cases for which we forced a planet to be located close to the positions of the features discussed in section 4. A planet located at $r_c = 0.184''$, $\theta_0 = 196.8°$ (in the orbital plane of the disk) reproduces the shape of the spiral and is also in accordance with the location of `f1` as seen in Fig. 4a, and b (green line). The analytical model of Eq. B.1, although simple, matches surprisingly well the "S" shape expected for a spiral density wave and triggering the accretion of gas onto a protoplanet. On the contrary, imposing the planet location at `f2` matches only the external part of the spiral S1 (blue line in Fig. 4a). For comparison the contours of the CO peak in the ALMA image is shown in Fig. 4b. Being localized at the surface, the spiral twists appear slightly offset from the perturbers positions (circles) which are in the midplane.

For the western spiral S2, since there is no obvious features nor strong signal which we can consider as a source, we blindly searched for the best matching model. The purple line in Fig. 4a corresponds to $r_c = 0.172''$, $\theta_0 = 6.0°$. This model reproduces well the external part of the western spiral, which presents a more diffuse aspect/broader shape than the eastern one, but it fails to match the innermost, eastern arm which is less tightly wound as it approaches the occulting spot ($0.1'' < r < 0.16''$).

6. Discussions

We provide further exploratory analysis of the two identified objects, reminding that they are both detected in polarimetry and total intensity.

The object labelled `f1` is fitting the source of the S1 spiral which at this location features an "S" shape, likely reminiscent of the stationary pattern composed of inward and outward spiral density waves excited by the gravitational potential of an accreting protoplanet (see Kley & Nelson 2012, for a review). The spirals are trailing as expected by theory, since the near side is the south-east part of the disk (Fukagawa et al. 2004) and the resolved velocity field (Piétu et al. 2005) implies that the disk rotates counterclockwise. However, it is not straightforward to determine if the signal is from pure scattering (polarized), or a mix of scattering and emission (usually unpolarized). Zhu (2015) has calculated the spectral energy distribution emitted from an accreting circumplanetary disk, which can be compared to our photometric measurements assuming the signal of `f1` is dominated by emission. The luminosity varies as the product of the planet mass with the accretion rate, and also depends on the inner radius of the circumplanetary disk. These three parameters necessarily lead to a high degree of degeneracy. Although it is difficult to overcome the ADI bias in total intensity measured for the particular case of `f1`, as it is not point-like, we measured a minimum contrast of 6.5×10^{-4} in the H band. If we assume moderate accretion rate of $10^{-8} M_\odot/\mathrm{yr}$ as in Zhu (2015), it translates into a planet mass of $4 - 13 M_J$. We note that the accretion rates estimated for PDS 70b are orders of magnitude lower (Haffert et al. 2019; Hashimoto et al. 2020), which then would imply stellar mass for `f1`. As a consequence, the flux of `f1` is likely not dominated by thermal emission.

On the contrary, the object `f2` is not directly associated to a spiral, so we assume its flux can be pure scattering. Mass constraints can be derived from dynamical argument. Indeed, the inner edge of the disk cavity at ~ 140 au can be sculpted by the
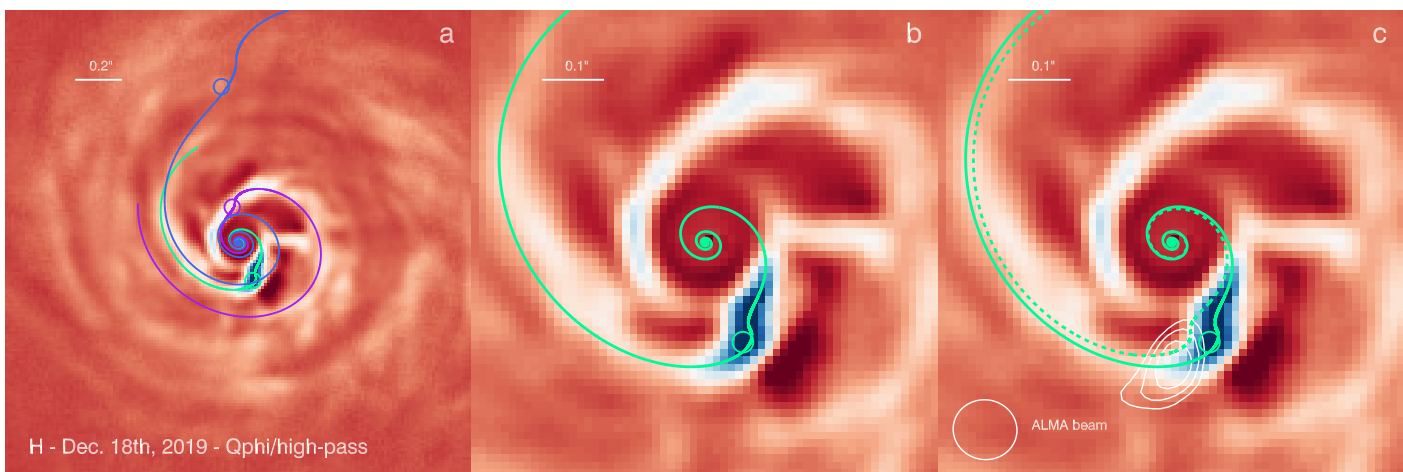
Fig. 4. Same data as Fig. 3 with three different models of spirals matching S1 (green and blue lines) and S2 (purple line). The positions of the perturbers are indicated with a circle (panel a). Panel b is a zoom in version of panel a, where only the best model reproducing the spiral twist in S1 is shown. In panel c, the contours of the CO map at the location of the candidate protoplanet are overlaid, together with the spiral model offset by 14.1° (dashed green line), corresponding to the 4-yr timelapse between ALMA and SPHERE observations.

chaotic zone of a planetary mass object. Assuming a circular orbit for the sake of simplicity, Wisdom (1980) provides a relation between the planet/star mass ratio, and the inner edge/planet distance ratio, from which we derived a mass of $\sim 3M_J$. The AB Aur cavity is very large, such that, if resulting from dynamical interplay with planets, several bodies including f1 should be involved.

Finally, the object f1 appears rotated counterclockwise from the CO peak in the ALMA image which, considering the stellar mass, the 4-yr interval, and the physical stellocentric distance of f1, is in excellent agreement with the expected rotation (14.1 ± 1.1° in the orbital plane) of the spiral due to the Keplerian motion of the protoplanet candidate (Fig. 4c). However, the peak of the CO emission is at a radial distance slightly larger than expected. There are a few technical reasons accounting for this difference which remain to be investigated thoroughly. Nevertheless, to our knowledge, this is the first time that we can confidently associate the rotation of a spiral pattern with the orbital motion of a planet candidate, which reinforces our confidence in the nature of the detected spiral twist.

To conclude, the SPHERE observations of AB Aur in scattered light combined to ALMA data in the thermal regime are providing strong evidence that we are actually witnessing ongoing planet formation revealed by its associated spiral arms. Further observations would be required to confirm this result and to derive better mass estimates for the potential planets.

References

Bae, J. & Zhu, Z. 2018, ApJ, 859, 118
Benisty, M., Juhasz, A., Boccaletti, A., et al. 2015, A&A, 578, L6
Beuzit, J. L., Vigan, A., Mouillet, D., et al. 2019, A&A, 631, A155
Boccaletti, A., Pantin, E., Lagrange, A. M., et al. 2013, A&A, 560, A20
Christiaens, V., Casassus, S., Perez, S., van der Plas, G., & Ménard, F. 2014, ApJ, 785, L12
Clampin, M., Krist, J. E., Ardila, D. R., et al. 2003, AJ, 126, 385
Claudi, R., Beuzit, J. L., Feldt, M., et al. 2008, in European Planetary Science Congress 2008, 875
de Boer, J., Langlois, M., van Holstein, R. G., et al. 2020, A&A, 633, A63
Delorme, P., Meunier, N., Albert, D., et al. 2017, in Proceedings of the SF2A, 347–361
DeWarf, L. E., Sepinsky, J. F., Guinan, E. F., Ribas, I., & Nadalin, I. 2003, ApJ, 590, 357
di Folco, E., Dutrey, A., Chesneau, O., et al. 2009, A&A, 500, 1065
Dohlen, K., Langlois, M., Saisse, M., et al. 2008, in Proc. SPIE, ed. I. S. McLean & M. M. Casali, 118
Dong, R., Zhu, Z., Fung, J., et al. 2016, ApJ, 816, L12
Dong, R., Zhu, Z., Rafikov, R. R., & Stone, J. M. 2015, ApJ, 809, L5
Fukagawa, M., Hayashi, M., Tamura, M., et al. 2004, ApJ, 605, L53
Fukagawa, M., Tamura, M., Itoh, Y., et al. 2006, ApJ, 636, L153
Gaia Collaboration, Brown, A. G. A., Vallenari, A., et al. 2018, A&A, 616, A1
Galicher, R., Boccaletti, A., Mesa, D., et al. 2018, A&A, 615, A92
Grady, C. A., Polomski, E. F., Henning, T., et al. 2001, AJ, 122, 3396
Grady, C. A., Woodgate, B., Bruhweiler, F. C., et al. 1999, ApJ, 523, L151
Gressel, O., Nelson, R. P., Turner, N. J., & Ziegler, U. 2013, ApJ, 779, 59
Haffert, S. Y., Bohn, A. J., de Boer, J., et al. 2019, Nature Astronomy, 3, 749
Hashimoto, J., Aoyama, Y., Konishi, M., et al. 2020, arXiv.org [2003.07922v1]
Hashimoto, J., Tamura, M., Muto, T., et al. 2011, ApJ, 729, L17
Isella, A., Natta, A., Wilner, D., Carpenter, J. M., & Testi, L. 2010, ApJ, 725, 1735
Juhasz, A., benisty, M., Pohl, A., et al. 2015, MNRAS, 451, 1147
Kadam, K., Vorobyov, E., Regály, Z., Kóspál, Á., & Ábrahám, P. 2019, ApJ, 882, 96
Kley, W. & Nelson, R. P. 2012, ARA&A, 50, 211
Li, D., Pantin, E., Telesco, C. M., et al. 2016, ApJ, 832, 18
Lomax, J. R., Wisniewski, J. P., Grady, C. A., et al. 2016, ApJ, 828, 2
Maire, A.-L., Langlois, M., Dohlen, K., et al. 2016, in Proc. SPIE, Vol. 9908, 990834
Milli, J., Mouillet, D., Lagrange, A. M., et al. 2012, A&A, 545, A111
Muto, T., Grady, C. A., Hashimoto, J., et al. 2012, ApJ, 748, L22
Oppenheimer, B. R., Brenner, D., Hinkley, S., et al. 2008, ApJ, 679, 1574
Pavlov, A., Möller-Nilsson, O., Feldt, M., et al. 2008, in Proc. SPIE, Vol. 7019, 39
Perrin, M. D., Schneider, G., Duchêne, G., et al. 2009, ApJ, 707, L132
Phuong, N. T., Dutrey, A., di Folco, E., et al. 2020, A&A, 635, L9
Piétu, V., Guilloteau, S., & Dutrey, A. 2005, A&A, 443, 945
Rafikov, R. R. 2002, ApJ, 569, 997
Rice, W. K. M., Lodato, G., & Armitage, P. J. 2005, MNRAS, 364, L56
Rivière-Marichalar, P., Fuente, A., Baruteau, C., et al. 2019, ApJ, 879, L14
Salyk, C., Herczeg, G. J., Brown, J. M., et al. 2013, ApJ, 769, 21
Schmid, H. M., Joos, F., & Tschan, D. 2006, A&A, 452, 657
Soummer, R., Pueyo, L., & Larkin, J. 2012, ApJ, 755, L28
Tang, Y.-W., Guilloteau, S., Dutrey, A., et al. 2017, ApJ, 840, 0
Tang, Y. W., Guilloteau, S., Piétu, V., et al. 2012, A&A, 547, A84
van Holstein, R. G., Girard, J. H., de Boer, J., et al. 2020, A&A, 633, A64
Wisdom, J. 1980, AJ, 85, 1122
Zhu, Z. 2015, ApJ, 799, 16

Appendix A: Complementary data

Appendix B: Expression of a spiral arm

According to the theory of density waves generated by a gravitational perturber (Rafikov 2002) in protoplanetary disks, Muto et al. (2012) proposed an approximate linear relation to describe the shape of a spiral $\theta(r)$, as a function of the planet location (r_c, θ_0) and disk properties, as follows:

$$
\begin{aligned}
\theta(r) \quad = \quad & \theta_0 - \frac{\mathrm{sgn}(r - r_c)}{h_c} \\
& \times \left[\left(\frac{r}{r_c} \right)^{1+\beta} \left\{ \frac{1}{1+\beta} - \frac{1}{1-\alpha+\beta} \left(\frac{r}{r_c} \right)^{-\alpha} \right\} \right. \\
& \left. - \left(\frac{1}{1+\beta} - \frac{1}{1-\alpha+\beta} \right) \right]
\end{aligned} \tag{B.1}
$$

where h_c is the disk aspect ratio at the planet location, α and β are the power-law exponents of the angular frequency and temperature profile dependence with r. In this paper, we assumed $\alpha = 1.5$ for Keplerian velocity, and $\beta = 0.25$ to account for the temperature profile which varies as $r^{-2\beta}$.

This formulation is now commonly used to interpret high contrast images in which spiral patterns are observed, but involves a number of assumptions, in particular that small grains observed in scattered light are coupled to the gas, and that a single planet induces a single spiral arm. This is obviously not always supported by hydro-dynamical simulations which result in much more complex morphologies. In a more realistic situation, a planet can produce several spiral arms (Dong et al. 2015), or planet formation should lead inevitably to multiple cores hence to manyfold spirals (Kadam et al. 2019).

Date UT	Filter	Fov rotation (°)	DIT (s)	N_{exp}	T_{exp} (s)	seeing ('')	τ_0 (ms)	Flux var. (%)	TN (°)
2019-12-18	IRDIS - H	29.6	32	160	5120	0.67 ± 0.09	7.1 ± 0.9	~2	−1.70
2020-01-17	IRDIS - K1K2	38.5	16	256	4096	0.71 ± 0.22	5.6 ± 1.1	~2	−1.77
2020-01-17	IFS - YJH	38.5	64	64	4096	0.71 ± 0.22	5.6 ± 1.1	~2	−1.77

Table A.1. Log of SPHERE observations indicating (left to right columns): the date of observations in UT, the filters combination, the amount of field rotation in degrees, the individual exposure time (DIT) in seconds, the total number of exposures, the total exposure time in seconds, the DIMM seeing measured in arcseconds, the correlation time τ_0 in milliseconds, the variation of the flux during the sequence in %, and the true north (TN) offset in degrees.
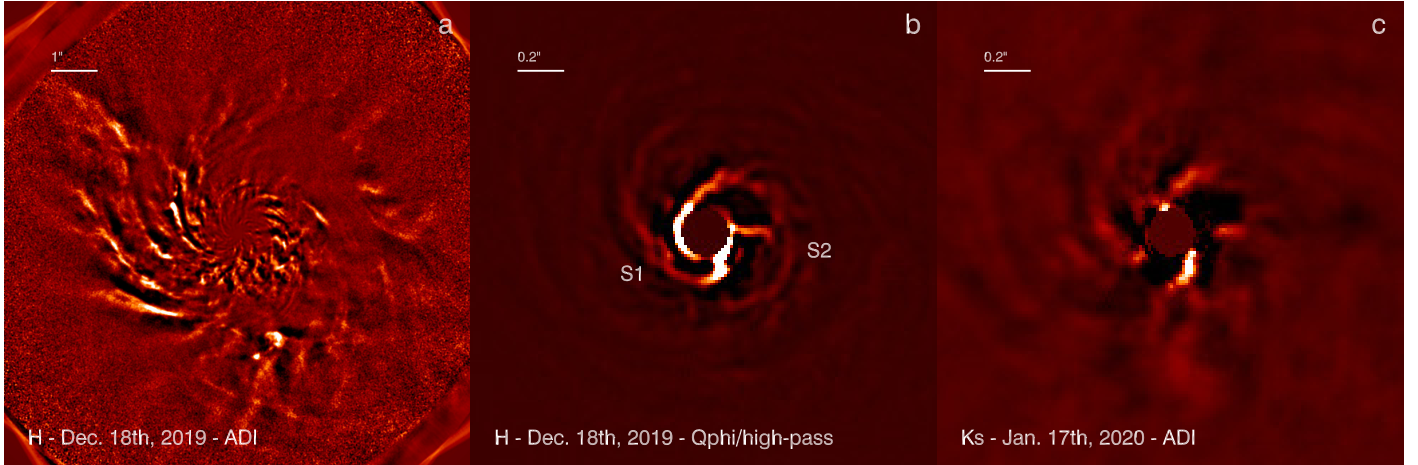
Fig. A.1. Complementary images of the AB Aur system. (a) ADI image (H band) in a large field of view (10'') multiplied with the square of the stellocentric distance. (b) high-pass filtering of the DPI image to enhance the spirals S1 and S2. (c) second epoch ADI observations in the K1K2 filters.